ANALYTICAL APPROACH TO FORMATION FLYING WITH LOW-THRUST RELATIVE SPIRAL TRAJECTORIES

Matthew Willis* **and Simone D'Amico†**

This work addresses the growing need for an intuitive, systematic approach to low-thrust formation flying by extending shape-based continuous thrust trajectory design methods to the relative motion of two spacecraft. There is growing interest in distributed space systems for their low costs, broad capabilities, and high redundancy. This trend introduces a new challenge for trajectory design when combined with the increasing prevalence of low-thrust, high specific impulse electric propulsion systems. That challenge is met herein with a geometrically intuitive, semi-analytical solution to the low-thrust problem. Beginning with the equations of relative motion of two spacecraft, an unperturbed chief and a continuously-thrusting deputy, a thrust profile is constructed which transforms the equations into a form that is solved analytically. The resulting relative trajectories are the family of sinusoidal spirals, which provide diversity for design and optimization based upon a single thrust parameter. Closed-form expressions are derived for the trajectory shape and time-of-flight for two prescribed relative velocity behaviors, and used to develop a novel patched-spirals trajectory design and optimization method. The example problem of a servicer spacecraft establishing and reconfiguring a formation around a target in geostationary earth orbit is used to demonstrate the application of the patched spirals technique as well as the advantages of the relative spiral trajectories over impulsive maneuvers. The sensitivity of the trajectory solutions to deviations from the underlying assumptions, uncertainties in the state, and errors in thrust are studied through high-fidelity simulation.

INTRODUCTION

The next generation of spacecraft architectures will be characterized by its increased utilization of distributed space systems and low-thrust, electric propulsion. Successful demonstration of formation flying in missions such as Orbital Express,[1] TanDEM-X,[2] and PRISMA[3] has opened the door to advanced mission concepts including distributed occulter/telescopes and on-orbit satellite servicing.[4] Simultaneously, the development of continuous low-thrust propulsion systems for interplanetary probes such as Deep Space 1[5] and Dawn[6] has stimulated the widespread adoption of ion and hall thrusters for satellite station-keeping.[7] This work addresses the problem created by the intersection of these trends, namely continuous low-thrust control of spacecraft formations. By adapting shape-based methods for low-thrust trajectory design to the relative motive motion of two spacecraft, the low-thrust formation-flying problem is recast in a purely analytical framework.

Past formation flying missions have employed chemical rockets and cold-gas thrusters for maneuvering. These propulsion systems can produce up to 100 N of thrust and achieve the required maneuver ΔV over a span of a few seconds.[8] Electric propulsion systems, on the other hand, produce thrusts on the order of 10 μN to 1 N and must operate continuously for a large portion of the orbit to achieve the required ΔV.[9] The tradeoff is that electric propulsion systems can achieve an order of magnitude improvement in specific impulse (Isp) over small chemical rockets. For their fuel efficiency and compact nature, electric propulsion systems are particularly valuable to the growing field of micro- and nanosatellites.

*PhD Candidate, Department of Mechanical Engineering, Stanford University, Durand Building, 496 Lomita Mall, Stanford, CA 94305.
†Professor, Department of Aeronautics and Astronautics, Stanford University, Durand Building, 496 Lomita Mall, Stanford, CA 94305.

Early studies in low-thrust relative motion by Lembeck and Prussing,[10] Carter,[11] and Guelman and Aleshin[12] focused on the problem of optimal rendezvous. Based on the primer vector theory of Lawden,[13] they examine rendezvous with unbounded thrust, bounded thrust, and constrained approach direction, respectively. Low-thrust formation control laws based on Lyapunov theory were introduced by de Queiroz et al.[14] and Schaub et al.,[15] to drive a formation toward a prescribed relative trajectory. The NetSat demonstration mission, which consists of four nanosatellites capable of low-thrust propulsion, has motivated further interest in this area.[16] For this mission, Steindorf et al. developed a controller using a reference governor based on relative orbit elements.[17] This approach merges the guidance and control problems into a path-planning problem in the relative orbit elements space. Bevilacqua and Lovell present an analytical approach to spacecraft relative guidance with constant thrust based on relative orbit elements and input shaping, a concept adapted from flexible structure control theory.[18]

Low-thrust trajectory design is generally formulated as a nonlinear optimization problem. Because numerical solvers may be highly sensitive to the search parameters, having a good initial guess is crucial. Shape-based methods provide one route to finding an initial guess, by analytically studying the thrust profile required to follow a prescribed trajectory. The first instance of this method was the study of the logarithmic spiral as a low-thrust, absolute trajectory by Bacon in 1959.[19] Other authors extended the method for the absolute motion of a single spacecraft with more general and useful shapes, such as the exponential sinusoid with variable flight path angle.[20] More recently, Roa showed that the thrust required by the logarithmic spiral trajectory can be extended to a family of generalized logarithmic spirals.[21]

The present investigation applies an approach analogous to these shape-based methods to the problem of low-thrust formation flying. Building upon recent work by the authors, it introduces a novel analytical framework for studying spacecraft relative motion and validates the results through sensitivity analysis in high-fidelity simulation.[22] The remainder of the paper is structured in four parts, beginning with a summary of key results in this area. First, the equations of relative motion are introduced and used to derive the sinusoidal spiral trajectory shape and thrust profile, along with explicit time of flight expressions for two relative velocity control schemes. Next, two strategies for patching together relative spiral trajectories are described. In the third section, these strategies are applied to the example problem of a servicer spacecraft visiting a target in geostationary earth orbit (GEO). The final section validates these developments by examining the sensitivity of the trajectory solution to departures from the underlying assumptions, errors in the relative state estimate, and thrust actuation errors.

THEORETICAL DEVELOPMENT

Equations of Relative Motion

To motivate and introduce the shape-based approach, the discussion begins with a review of the underlying theory and key developments from recent work. The motion of a deputy spacecraft relative to a chief orbiting a central body is governed by the difference of their respective fundamental orbital differential equations as

$$\frac{^{IJK}d^2}{dt^2}\boldsymbol{\delta}\mathbf{r} = \mu\left(\frac{\mathbf{r_c}}{r_c^3} - \frac{\mathbf{r_c}+\boldsymbol{\delta}\mathbf{r}}{||\mathbf{r_c}+\boldsymbol{\delta}\mathbf{r}||^3}\right) + \mathbf{u_d} - \mathbf{u_c} \tag{1}$$

where $\mathbf{r_c}$ and $\mathbf{r_d}$ are the position vectors from the central body to the chief and deputy, respectively, $\mathbf{u_c}$ and $\mathbf{u_d}$ are their control acceleration vectors, and $\boldsymbol{\delta}\mathbf{r} = \mathbf{r_d} - \mathbf{r_c}$ is the relative position vector. Although the derivatives in Eq. (1) are taken with respect to an inertial reference frame IJK, the relative motion is measured in a frame rotating with the orbit of the chief spacecraft. Often designated the radial-transverse-normal (RTN) frame, it may be associated with basis vectors $\hat{\mathbf{r}}$, $\hat{\boldsymbol{\theta}}$, and $\hat{\mathbf{n}}$ where $\hat{\mathbf{r}}$ points radially from the central body to the chief, $\hat{\mathbf{n}}$ is parallel to the chief's orbital angular velocity vector $\boldsymbol{\omega}$, and $\hat{\boldsymbol{\theta}}$ is the transverse vector formed from $\hat{\mathbf{n}} \times \hat{\mathbf{r}}$. This basis is illustrated schematically in Figure 1 for coplanar motion. Also shown is the relative velocity vector $\boldsymbol{\delta}\mathbf{v}$ defined by

$$\boldsymbol{\delta}\mathbf{v} \equiv \frac{^{RTN}d}{dt}\boldsymbol{\delta}\mathbf{r} \tag{2}$$

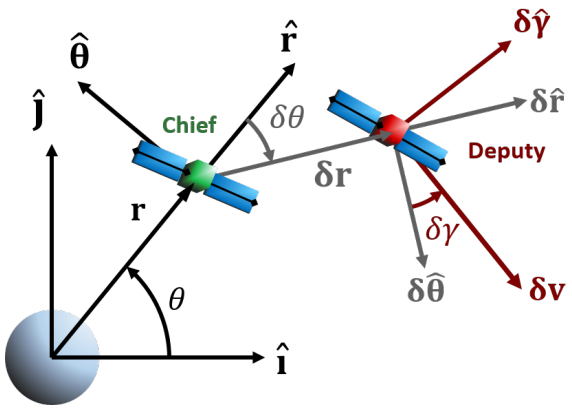

Figure 1. Geometry for studying the motion of a deputy spacecraft (red) relative to a chief (green).

Using the definition of the relative velocity and the chief's orbital angular velocity vector $\boldsymbol{\omega}$, the second-order ordinary differential equation (ODE) in Eq. (1) becomes a system of first-order ODEs given by Eq. (2) and

$$\frac{^{RTN}d}{dt}\boldsymbol{\delta v} + \frac{^{RTN}d\boldsymbol{\omega}}{dt} \times \boldsymbol{\delta r} + 2\boldsymbol{\omega} \times \boldsymbol{\delta v} + \boldsymbol{\omega} \times (\boldsymbol{\omega} \times \boldsymbol{\delta r}) = \mu \left(\frac{\mathbf{r_c}}{r_c^3} - \frac{\mathbf{r_c} + \boldsymbol{\delta r}}{||\mathbf{r_c} + \boldsymbol{\delta r}||^3} \right) + \mathbf{u_d} - \mathbf{u_c} \tag{3}$$

Equations (2) and (3) provide the most general description of the relative motion of the deputy with respect to the chief, without explicit dependence on the deputy's absolute state or an inertial reference frame. If the chief is in an unperturbed circular orbit, the direction of $\boldsymbol{\omega}$ is constant, its magnitude is n, and $\mathbf{u_c} = \mathbf{0}$. After adopting this assumption there is no further need to distinguish between chief and deputy thrusts, so the deputy's thrust will be referred to as $\mathbf{u}$ henceforth.

The authors introduced the polar coordinate representations of the relative state illustrated in Figure 1 to convert Eqs. (2) and (3) from vector form to a scalar form suitable for shape-based analysis.[22] The deputy's relative position is characterized by $\delta r \equiv \|\boldsymbol{\delta r}\|$ and the angle $\delta\theta$, which is measured from $\hat{\mathbf{r}}$ to $\boldsymbol{\delta r}$ with sense opposite to the chief's orbital angular momentum vector. The relative velocity is characterized by $\delta v \equiv \|\boldsymbol{\delta v}\|$ and the relative flight path angle $\delta\gamma$, which is measured from $\boldsymbol{\delta\hat{\theta}}$ to $\boldsymbol{\delta v}$ with sense parallel to the chief's angular velocity vector. For this discussion, only motion in the chief's orbit plane is considered.

Taking the $\boldsymbol{\delta\hat{r}}$ and $\boldsymbol{\delta\hat{\theta}}$ components of Eq. (2) leads to the scalar differential equations that govern the time-evolution of the relative position variables as

$$\dot{\delta r} = \delta v \sin\delta\gamma \tag{4}$$

$$\dot{\delta\theta} = \frac{\delta v}{\delta r}\cos\delta\gamma \tag{5}$$

Next, taking the $\boldsymbol{\delta\hat{v}}$ and $\boldsymbol{\delta\hat{\gamma}}$ components of Eq. (3), expanding $\|\mathbf{r_c} + \boldsymbol{\delta r}\|^{-3}$ in powers of $\delta r/r_c$, and dropping higher-order terms for small separations leads to the equations

$$\dot{\delta v} = 3n^2\delta r \sin(\delta\gamma - \delta\theta)\cos\delta\theta + \mathbf{u}\cdot\boldsymbol{\delta\hat{v}} \tag{6}$$

$$\delta v\left(\dot{\delta\gamma} - \dot{\delta\theta}\right) = 3n^2\delta r\cos(\delta\gamma - \delta\theta)\cos\delta\theta - 2n\delta v + \mathbf{u}\cdot\boldsymbol{\delta\hat{\gamma}} \tag{7}$$

governing the relative velocity variables. The system of ODEs in Eqs. (4) through (7) is mathematically equivalent to the in-plane Hill-Clohessy-Wiltshire equations.[23]

Relative Spiral Geometry

By judicious choice of the deputy's thrust profile $\mathbf{u}$, the authors derived a closed-form solution for the trajectory shape in the chief's RTN frame.[22] Due to the choice of state representation, the trajectory shape is controlled by Eq. (7) with explicit dependence only on the $\boldsymbol{\delta}\hat{\boldsymbol{\gamma}}$ component of thrust. In principle, a thrust profile could be derived to satisfy any desired trajectory shape. This investigation follows the inverse approach, prescribing a thrust profile that renders the governing equations in solvable form while retaining solution diversity for design and optimization. The thrust profile was chosen to impose a proportionality between $\dot{\delta\gamma}$ and $\dot{\delta\theta}$, controlled by the thrust parameter ξ. Examination of Eq. (7) leads to the required thrust profile

$$\mathbf{u} \cdot \boldsymbol{\delta}\hat{\boldsymbol{\gamma}} = \delta v \left[(\xi - 1) \frac{\delta v}{\delta r} \cos \delta\gamma + 2n \right] - 3n^2 \delta r \cos \delta\theta \cos(\delta\gamma - \delta\theta) \tag{8}$$

Because all terms in Eq. (8) scale as $n^2 \delta r$, the maximum control thrust with separations smaller than 10 km will vary from mN/kg in low earth orbit to μN/kg in GEO. This thrust range overlaps with that of current electric propulsion systems, so the control law selected is potentially realizable.

Using the thrust profile from Eq. (8) in Eq. (7), one obtains an expression for $\delta\gamma$ in terms of $\delta\theta$ and initial conditions. Combining this relationship with Eqs. (4) and (5) leads to the closed form solution for the trajectory shape

$$\delta r = \begin{cases} \delta r_0 \exp\left[(\delta\theta - \delta\theta_0) \tan \delta\gamma \right] & \xi = 0 \\ \dfrac{\delta r_m}{\cos^{1/\xi}\left[\xi(\delta\theta - \delta\theta_m) \right]} & \xi \neq 0 \end{cases} \tag{9}$$

The geometric parameters δr_m and $\delta\theta_m$ have been introduced to eliminate explicit dependence on the initial conditions. These quantities may be obtained from the state variables at any point on the trajectory using

$$\delta r_m = \delta r \cos^{1/\xi} \delta\gamma \tag{10}$$

$$\delta\theta_m = \delta\theta - \frac{\delta\gamma}{\xi} \tag{11}$$

Equation (9) describes the family of sinusoidal spirals, whose diversity is sampled in Figure 2. For $\xi = 0$, the relative flight path angle $\delta\gamma$ is constant and the deputy follows either a logarithmic spiral or a circular arc centered on the chief. The trajectory spirals outward if $\delta\gamma > 0$ and inward if $\delta\gamma < 0$. For $\xi < 0$, $\delta\gamma$ decreases as $\delta\theta$ increases, the trajectory solution is bounded, and δr_m represents the maximum separation between chief and deputy. For $\xi > 0$, $\delta\gamma$ increases with $\delta\theta$, the solution is unbounded, and δr_m defines the minimum separation. The polar angle $\delta\theta$ is restricted to the range $\delta\theta_m \pm \pi/2|\xi|$, so for ξ between -0.5 and 0.5 the trajectory fully encircles the chief. For ξ outside of this range, the trajectory either converges to the chief or diverges to infinity without crossing itself.

As Figure 2 illustrates, the family of sinusoidal spirals includes several shapes familiar from classical geometry.[24] These include the logarithmic spiral and circle corresponding to $\xi = 0$ in Figure 2(a). The spiral with $\xi = -0.5$ in Figure 2(b) is a cardioid, while that with $\xi = 0.5$ in Figure 2(c) is a parabola with the chief on the directrix. Figure 2(d) shows spirals for more extreme values of the thrust parameter, including a straight line for $\xi = 1$, a rectangular hyperbola centered on the chief for $\xi = 2$, a circle passing through the chief for $\xi = -1$, and the Lemniscate of Bernoulli for $\xi = -2$.

Solution Dynamics

Motion along the trajectory is described by δv and therefore governed by Eq. (6), with explicit dependence on the $\boldsymbol{\delta}\hat{\mathbf{v}}$ component of thrust. This study considers two relative velocity control schemes. The first maintains a constant ratio of δv to δr, based on the result of linear relative motion theory that the relative speed varies in proportion to the size of the relative orbit. The second maintains a constant δv to enable a broader range of dynamic behavior.

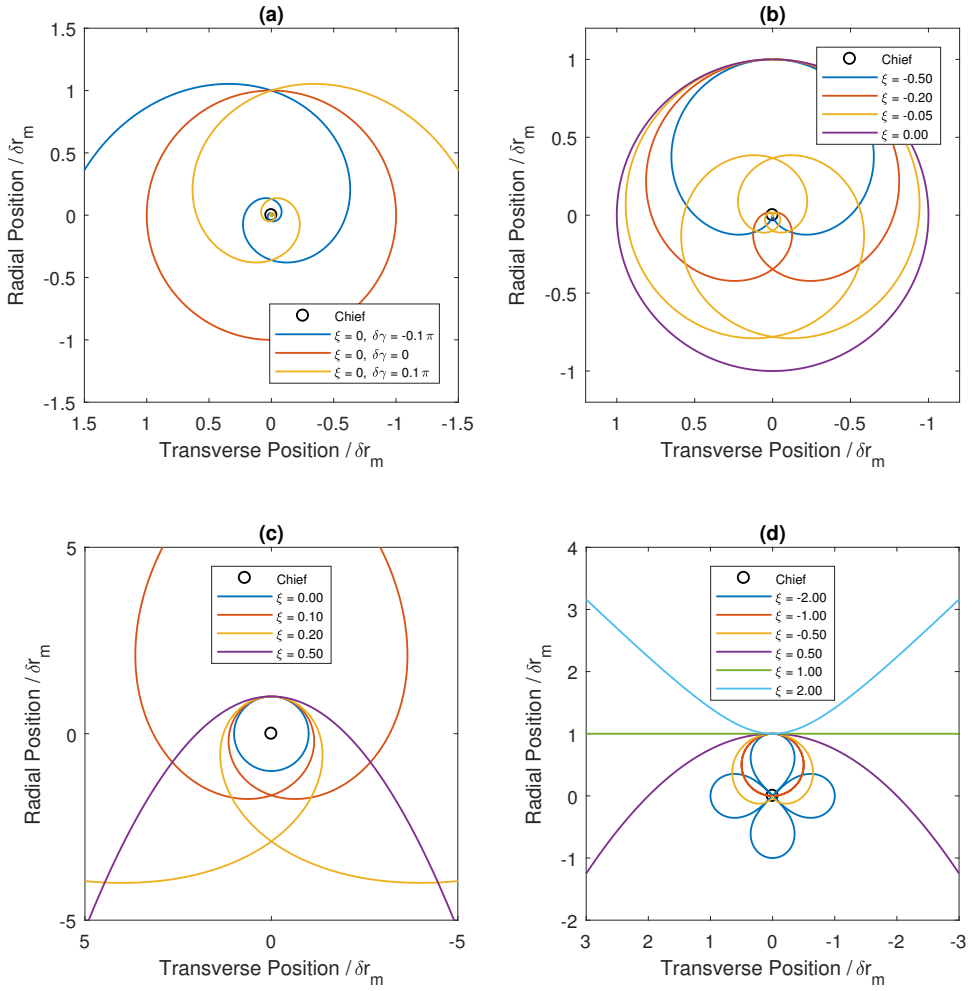

Figure 2. Geometry of relative spiral trajectory solutions for select values of ξ and $\delta\theta_m = 0$. (a) $\xi = 0$, (b) $-0.5 \leq \xi \leq 0$, (c) $0 \leq \xi \leq 0.5$, (d) $\xi \leq -0.5$ and $\xi \geq 0.5$.

Constant $\delta v/\delta r$ The requirement for maintaining a constant ratio of δv to δr is that

$$\frac{d}{dt}\left(\frac{\delta v}{\delta r}\right) = \frac{\dot{\delta v}}{\delta r} - \frac{\delta v}{\delta r^2}\dot{\delta r} = 0 \tag{12}$$

Substituting Eqs. (4) and (6) into Eq. (12) and applying initial conditions leads to the $\boldsymbol{\delta\hat{v}}$ measure of thrust

$$\mathbf{u} \cdot \boldsymbol{\delta\hat{v}} = \delta v \frac{\delta v_0}{\delta r_0} \sin\delta\gamma - 3n^2\delta r \cos\delta\theta \sin(\delta\gamma - \delta\theta) \tag{13}$$

The two terms in Eq. (13) are comparable in magnitude and whether they add or subtract depends upon the values of $\delta\gamma$ and $\delta\theta$ at a given time.

Thus far, the equations of motion have been solved by replacing time with $\delta\theta$ as the independent variable. However, a sense of time is required for trajectory design. The time of flight is obtained by integration of Eq. (5) using the known dependences of δv, δr, and $\delta\gamma$ on $\delta\theta$. This leads to the analytical expression

$$TOF = \begin{cases} \dfrac{\delta r_0}{\delta v_0} \dfrac{\delta\theta_f - \delta\theta_0}{\cos\delta\gamma_0} & \xi = 0 \\ \dfrac{\delta r_0}{\delta v_0}\left[\ln\delta r + \dfrac{1}{\xi}\ln(\sin\delta\gamma + 1)\right]_0^f & \xi \neq 0 \end{cases} \tag{14}$$

which takes on a different form based on whether $\delta\gamma$ is constant or variable.[22]

Constant δv To maintain a constant relative velocity, the control thrust needs only compensate for the component of the differential gravitational force that is tangential to the curve. From Eq. (6), the resulting thrust profile in the $\boldsymbol{\delta}\hat{\mathbf{v}}$ direction is given by

$$\mathbf{u} \cdot \boldsymbol{\delta}\hat{\mathbf{v}} = -3n^2\delta r \cos\delta\theta \sin(\delta\gamma - \delta\theta) \tag{15}$$

and follows the same $n^2\delta r$ scaling as the thrust profiles considered previously.

Again, the dynamics governing $\dot{\delta\theta}$ in Eq. (5) can be directly integrated in terms of the trajectory shape in Eq. (9) and known behavior of δr, δv, and $\delta\gamma$ to obtain the time of flight. Because δv is constant, time of flight is proportional to the path length. This may be understood geometrically for the two $\xi = 0$ cases. For a circular arc, it is the subtended angle divided by the angular velocity. For a logarithmic spiral, it is the change in separation divided by the constant measure of velocity toward or away from the chief. These relationships are expressed mathematically as

$$TOF = \begin{cases} \dfrac{\delta r_0}{\delta v_0}(\delta\theta_f - \delta\theta_0) & \delta\gamma_0 = 0 \\ \dfrac{\delta r_f - \delta\theta_0}{\delta v_0 \sin\delta\gamma_0} & \delta\gamma_0 \neq 0 \end{cases} \tag{16}$$

For the general case of $\xi \neq 0$, the path length integral is more complicated and time of flight must be expressed in terms of the Gauss hypergeometric function ${}_2F_1(a, b; c; z)$ as

$$TOF = \frac{1}{\xi}\frac{\delta r_m}{\delta v_0}\left[\sin\delta\gamma\, {}_2F_1\left(\frac{1}{2}, 1 + \frac{1}{2\xi}; \frac{3}{2}; \sin^2\delta\gamma\right)\right]_0^f \tag{17}$$

For many special cases, including the classical geometric figures described in section 2.2 above, Eq. (17) reduces to more familiar mathematical functions. A list of such cases is omitted here for brevity but may be found in standard handbooks of mathematical functions such as Abramowitz and Stegun.[25]

PATCHED SPIRALS

Mission planning requires that sinusoidal spiral maneuvers be patched between periods without thrust and may require that multiple spirals be patched to accomplish the desired objective. For relative orbit control in formation flying missions, it is expected that the patched trajectories share a common reference point. However, one may add degrees of freedom to the trajectory design space by patching spirals with distinct reference points, enabling absolute orbit control. These problems are addressed in succession.

Relative Orbit Control

Consider first the scenario of the deputy spacecraft performing low-thrust maneuvers in the vicinity of a chief that is on a circular absolute orbit. At the beginning and end of any relative spiral maneuver, the spiral trajectory must be patched to the natural motion. Furthermore, the maneuver itself may consist of a sequence of relative spiral trajectories with different values of the thrust parameter ξ. In either case, the position and velocity state of the deputy relative to the chief must not change across the patch, so that

$$\begin{aligned} \delta r_+ &= \delta r_- \\ \delta\theta_+ &= \delta\theta_- \\ \delta v_+ &= \delta v_- \\ \delta\gamma_+ &= \delta\gamma_- \end{aligned} \tag{18}$$

A fundamental distinction between the methods of patched conics familiar from classical orbital mechanics and the method of patched spirals is that here both position and velocity must be constant across the patch. Discontinuities in the velocity magnitude or direction would imply an impulsive maneuver. While the thrust magnitude may change discontinuously, it cannot be an impulse.

Absolute Orbit Control

With the preceding formulation, the range of motion is restricted to the trajectories defined in Eq. (9) over a domain limited by the propulsion system's ability to supply the thrust prescribed by Eqs. (8), (13), and (15). Introducing the notion of the virtual chief as a reference point dramatically increases the scope.[26] Because the chief is not bound to a physical object, its location may be altered to allow for control of the deputy's absolute orbit by patching relative spiral trajectories. The conditions in Eq. (18) are void without a common reference point, and a new set of patching conditions must be introduced from continuity of the absolute position and inertial velocity of the deputy. Expressing the inertial velocity in terms of its radial and transverse measures in the deputy's RTN basis, the new constraints are

$$\begin{aligned} r_{d+} &= r_{d-} \\ \theta_{d+} &= \theta_{d-} \\ v_{dr+} &= v_{dr-} \\ v_{dt+} &= v_{dt-} \end{aligned} \tag{19}$$

These quantities are related to the relative motion variables in vector form by

$$\mathbf{r_d} = \mathbf{r_c} + \boldsymbol{\delta}\mathbf{r} \tag{20}$$

$$\mathbf{v_d} = \mathbf{v_c} + \boldsymbol{\delta}\mathbf{v} + \boldsymbol{\omega} \times \boldsymbol{\delta}\mathbf{r} \tag{21}$$

To unpack these equations, take their dot products with the chief's $\hat{\mathbf{r}}$ and $\hat{\boldsymbol{\theta}}$ basis vectors and solve for the inertial velocity components. The resulting scalar conditions are

$$r_d \cos(\theta_c - \theta_d) = r_c + \delta r \cos\delta\theta \tag{22}$$

$$r_d \sin(\theta_c - \theta_d) = \delta r \sin\delta\theta \tag{23}$$

$$v_{dr} r_d = \delta v \left[r_c \sin(\delta\gamma - \delta\theta) + \delta r \sin\delta\gamma \right] \tag{24}$$

$$v_{dt} r_d = n r_d^2 - \delta v \left[r_c \cos(\delta\gamma - \delta\theta) + \delta r \cos\delta\gamma \right] \tag{25}$$

Equations (22) through (25) constitute the mapping between absolute and relative motion needed to enforce the conditions in Eq. (19) given $r_{c\pm}$ and $\theta_{c\pm}$.

A variant of this patching problem is the boundary-value problem in which one seeks the relative states and intervening reference point for given initial and final absolute states. To approach this problem, first eliminate θ_d and θ_c from the parameter set by adding the squares of Eqs. (22) and (23) as

$$r_d^2 = r_c^2 + \delta r^2 + 2 r_c \delta r \cos\delta\theta \tag{26}$$

There are then nine unknowns, comprised of r_c and the initial and final relative states. Equations (24), (25), and (26) provide six constraints when considered at the two boundary conditions. Another two constraints are provided by the velocity profile and the linear relationship between $\delta\gamma$ and $\delta\theta$. The final constraint is supplied by the trajectory shape from Eq. (9). In terms of the relevant variables, this becomes

$$\frac{\delta r_f}{\delta r_0} = \begin{cases} \exp\left[(\delta\theta_f - \delta\theta_0) \tan\delta\gamma \right] & \xi = 0 \\ \left(\dfrac{\cos\delta\gamma_0}{\cos\delta\gamma_f} \right)^{\frac{1}{\xi}} & \xi \neq 0 \end{cases} \tag{27}$$

Exact solutions to this nonlinear system may be obtained with constant relative speed in the important special case of zero radial inertial velocity components at the initial and final states. That is, when the patch points are apses of the absolute orbit. For most scenarios relevant to relative spiral patching, the radial velocities will be small and these results provide a good starting point for numerical solution of the full system.

Combining Eq. (24) with v_{dr} set to 0 and Eq. (26) leads to the analytical expression for the mean motion of the reference orbit

$$n = \frac{v_{dt0} + v_{dtf}}{r_{d0} + r_{df}} \tag{28}$$

from which r_c may be calculated as $\sqrt[3]{\mu/n^2}$. Expressions for the constant relative speed δv may be found from Eqs. (25) and (28) at either of the boundary states as

$$\delta v = |n r_d - v_{dt}| \tag{29}$$

Up to this point in the analysis, no restrictions have been placed on the relative spiral shape. The results in Eqs. (28) and (29) follow from the choice of constant δv control. To proceed, the relative spiral geometry must be invoked. The solution takes on different forms depending on whether $\delta\gamma$ is constant or varying. In the $\xi = 0$ case, $\delta\gamma$ is constant and the variables $\delta\theta_f$, $\delta\gamma$, δr_0, and δr_f can all be related to $\delta\theta_0$. Inserting these relationships into the $\xi = 0$ trajectory shape expression in Eq. (27), the system is reduced to solving for $\delta\theta_0$ in the single transcendental equation

$$\frac{\delta r_f}{\delta r_0} = \frac{\sin(\delta\theta_f - \delta\gamma)}{\sin(\delta\theta_0 - \delta\gamma)} = \exp\left[(\delta\theta_f - \delta\theta_0)\tan\delta\gamma\right] \tag{30}$$

For $\xi \neq 0$, $\delta\gamma$ differs at the initial and final states, adding an additional unknown and constraint. The system reduces to solving for the unknowns $\delta\theta_0$ and $\delta\theta_f$ in the two transcendental equations

$$\frac{\delta r_f}{\delta r_0} = \frac{\sin(\delta\theta_f - \delta\gamma_f)}{\sin(\delta\theta_0 - \delta\gamma_0)} \frac{\sin\delta\gamma_0}{\sin\delta\gamma_f} = \left(\frac{\cos\delta\gamma_0}{\delta\gamma_f}\right)^{\frac{1}{\xi}} \tag{31}$$

$$\delta\gamma_f - \delta\gamma_0 = \xi(\delta\theta_f - \delta\theta_0) \tag{32}$$

where $\delta\gamma_i$ is expressed in terms of $\delta\theta_i$ using Eq. (24). The exact solution for patching a relative spiral trajectory between a given set of r_{d0}, r_{df}, v_{dt0}, and v_{dtf} with $v_{dr0} = v_{drf} = 0$ is obtained by the following steps. First, n is calculated directly from Eq. (28) and r_c from the definition of n, and δv from Eq. (29) and n. Based on a choice of ξ, either Eq. (30) is solved iteratively for $\delta\theta_0$ or Eqs. (31) and (32) are solved simultaneously for $\delta\theta_0$ and $\delta\theta_f$. If v_{dr0} or v_{drf} is nonzero, this procedure may be used to find an initial guess for numerically solving the full set of constraints in Eqs. (24) through (26) at the initial and final states and Eq. (27).

SAMPLE APPLICATION: GEO SERVICER MISSION

The notional satellite servicing mission scenario developed by NASA Goddard will serve as a perfect test case for demonstrating the utility of patched spirals.[27] The mission consists of a servicer spacecraft approaching a noncooperative target in GEO, inserting into a static safety ellipse, and executing a rendezvous with the target to refuel, repair, or boost the target into a disposal orbit.

Two modifications are made from the reference mission scenario for illustrative purposes. First, the safety ellipse is projected onto the target's orbital plane to accommodate the coplanar framework being considered. In a real mission, the ellipse would be tilted with respect to the target's orbital plane so that drift due to a small difference in semimajor axis would not lead to a collision risk. The small-out-of-plane velocity component required to achieve this relative state could be accomplished with minor adaptation of the thrust profile. However continuous-thrust control of the out-of-plane motion is saved for future discussion. To distinguish the closed, elliptical relative trajectories in the absence of control thrust from the controlled motions being considered, they will be referred to henceforth as passive ellipses. The second modification replaces the final rendezvous and capture phase of the scenario with a reconfiguration of the relative orbit size, equivalent to reducing the relative eccentricity vector. In the modified scenario, the servicer is initially in a large passive ellipse around the target for space situational awareness observations, then reduces the size of the passive ellipse for accurate pose estimation of the target before performing a rendezvous maneuver or departing for a new target.

Orbit Raising and Formation Establishment

At the start of the mission scenario, the servicer spacecraft is in a near-circular absolute orbit in the same plane as and approximately 30 km below the target. Figure 3 illustrates the series of maneuvers used to place the servicer in a passive ellipse around the target. Due to the initial difference in semimajor axis for the two spacecraft, the servicer drifts toward the target. Once sufficient angles-only navigation observations have been collected for the navigation filter to converge at this large separation, the deputy maneuvers into a new holding orbit 5 km below the target's orbit. With this smaller separation, the drift is slower and a more accurate state estimate may be obtained before the servicer maneuvers into a third holding orbit 1.5 km below the target. The final maneuver establishes the formation by placing the deputy into a passive elliptical relative orbit with a semiminor axis of 300 m. In the reference scenario, these maneuvers are accomplished with impulsive thrust. The remainder of this section will show that the techniques described above for patching trajectories with distinct reference points may be used to plan these maneuvers with continuous-thrust, relative spiral trajectories.

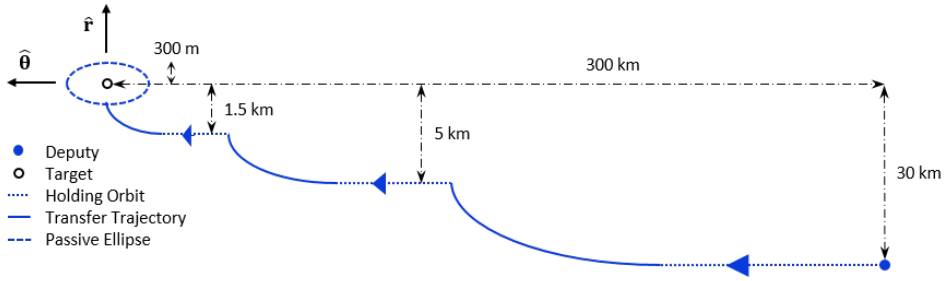

Figure 3. Formation establishment phase of GEO servicer mission scenario in RTN frame of target.

In the first two maneuvers of the sequence, the servicer changes its semimajor axis with no net change in eccentricity. As a geometrically intuitive starting point for spiral patching, one may consider placing the virtual chief midway between the initial and final holding orbits. When the deputy is directly below the chief on the first holding orbit, the relative speed in the RTN frame is related to their separation by

$$\delta v = \frac{3}{2} n \delta r \tag{33}$$

At its lower altitude, the deputy advances faster than the chief and the relative velocity is parallel to the chief's velocity vector. The relationship between δr and δv in Eq. (33) also applies to the case when the deputy is directly above the chief, but the relative velocity is then antiparallel to the chief's velocity vector, as Figure 4(a) illustrates. The transfer between concentric circular orbits may then be treated as a symmetrical trajectory in the RTN frame of a circular reference orbit midway between the departure and destination orbits. It is easy to imagine patching a semicircular relative trajectory between these initial and final states (cf. Figure 2 and Figure 4(a)). This corresponds to a relative spiral with $\xi = 0$ and $\delta\gamma = 0$. Because the separation is constant, the two relative speed control strategies lead to the same result.

The circular arc is the easiest relative spiral trajectory to understand, but it is not the only solution spiral for this transfer. Any spiral that sweeps at least π radians of $\delta\theta$ before reaching an asymptote could be used. Although the simple geometric intuition used to develop the $\xi = 0$ case cannot be readily applied for $\xi \neq 0$, the initial and final flight path angles for this transfer are zero so the exact solution can be obtained form the simplified constraints in Eqs. (28) through (32). Unlike the circular arc, the solution for general ξ will have variable δr and the two $\mathbf{u} \cdot \boldsymbol{\delta}\hat{\mathbf{v}}$ strategies will not produce the same motion. Solving Eqs. (30) through (32) for a range of ξ values allows for optimization over a cost function such as ΔV, as Figure 4(b) shows. The vertical axis is ΔV referenced to the value for the $\xi = 0$ case. The correspondence of the $\xi = 0$ case for both control schemes ensures a common scale for both curves. This plot was generated for the transfer between circular orbits 30 km and 5 km below GEO, but the shape of the curve is not strongly

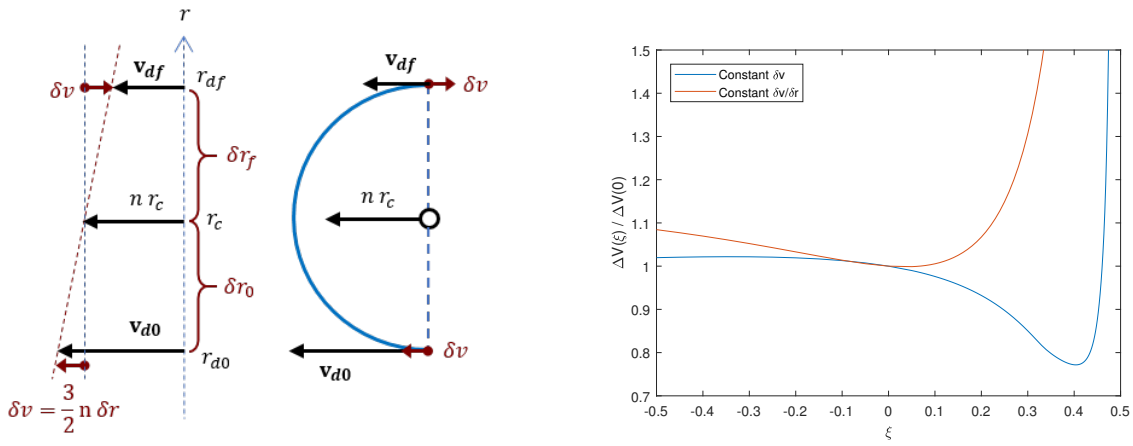

(a) Geometric construction of $\xi = 0$ case.

(b) ΔV-Optimization over a range of ξ.

Figure 4. Geometric development and optimization of relative spiral transfer with change in semimajor axis and no change in eccentricity.

dependent on the change in altitude so long as $\Delta r_d / r_c < 10^{-3}$. With the $\mathbf{u} \cdot \boldsymbol{\delta}\hat{\mathbf{v}}$ profile for constant δv, a 20% improvement in ΔV over the $\xi = 0$ case may be achieved using $\xi = 0.41$. This minimum represents a balance between time of flight and trajectory shaping costs. Lower values of ξ demand more control effort to shape the trajectory whereas higher values of ξ stretch the relative trajectory in the along-track direction and increase the maneuver duration. The sharp increase in ΔV as ξ approaches 0.5 is due to the inability of spirals with $\xi > 0.5$ to be tangent to both circular orbits.

The final maneuver in the sequence of Figure 3 requires a change of eccentricity as well as semimajor axis. To achieve passive elliptical motion in the target's RTN frame, the servicer must match its final semimajor axis to that of the target. For this analysis, the insertion point is assumed to be at perigee of the final orbit, corresponding to the point of the passive ellipse directly below the target. At this position, the separation is equal to the semiminor axis δr_E of the passive ellipse and the relative velocity is related to this separation by

$$\delta v = 2n\delta r_E \tag{34}$$

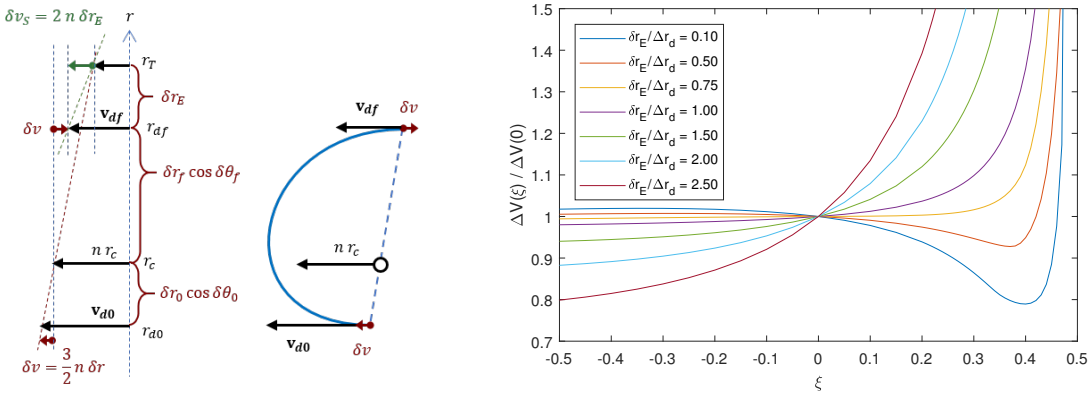

(a) Geometric construction of $\xi = 0$ case.

(b) ΔV-Optimization over a range of ξ.

Figure 5. Geometric development and optimization of relative spiral insertion into a passive ellipse with semiminor axis $\delta \mathbf{r_E}$.

The difference of $1/2\, n\delta r$ between Eqs. (33) and (34) accounts for the excess kinetic energy needed at perigee to reach apogee. If this velocity is transformed to the reference frame of a chief spacecraft located between the initial and final altitudes, the final relative speed will be slower than it would be with no change in eccentricity. To achieve this, the constant δv control strategy must be used and the chief placed below the mean altitude of the transfer to allow for δv windup in accordance with Eq. (28). This situation is illustrated schematically in Figure 5(a). An exact solution can be obtained from the constraints in Eqs. (28) through (32). Figure 5(b) generalizes the constant δv curve in Figure 4(b) to include change in eccentricity. The shape of the curve is a strong function of the ratio of δr_E to the radial span of the transfer Δr_d and no single-pass transfers of this type are possible for $\delta r_E > 3\Delta r_d$. For the prescribed insertion to a passive ellipse with 300 m semiminor axis from a holding orbit 1.5 km below the target, $\delta r_E/\Delta r_d = 0.25$ and the ΔV-minimizing value of ξ is 0.38.

Using appropriate values of the thurst parameter for the three maneuvers, the orbit-raising sequence can be simulated. The resulting trajectory with equally-distributed drift times is shown in Figure 6, along with the equivalent trajectory accomplished using impulsive Hohmann transfers. A total of 3.3 days is needed to complete the orbit raising and passive ellipse insertion. Table 1 compares performance measures for the relative-spiral and impulsive maneuvers. Although kinematic inefficiency increases the ΔV requirement for the low-thrust trajectory as compared to the impulsive case, the higher specific impulse of electric propulsion systems gives the relative spiral trajectory better performance in terms of propellant mass. In practice this mass savings would increase the number of targets that the servicer spacecraft could visit before retiring or refueling.

Two important factors to consider for continuous-thrust trajectory design are the maximum thrust required and the variation of the thrust level. For electric propulsion systems, the thrust is directly related to the power required, so the maximum thrust will be limited by the spacecraft's power supply. Furthermore, a

Table 1. Performance comparison for GEO servicer orbit raising maneuvers.

	Impulsive Thrust (Isp 300 s)		Low-Thrust Relative Spiral (Isp 2000 s)		
Maneuver	ΔV (m/s)	Propellant (mg/kg s/c)	ΔV (m/s)	Propellant (g/kg s/c)	Max Thrust (μN/kg)
25 km raise	0.91	311	2.36	120	70.2
3.5 km raise	0.13	43	0.33	16.7	9.8
Ellipse insertion	0.05	19	0.13	6.7	3.9
Total	1.094	0.372	2.814	0.191	-

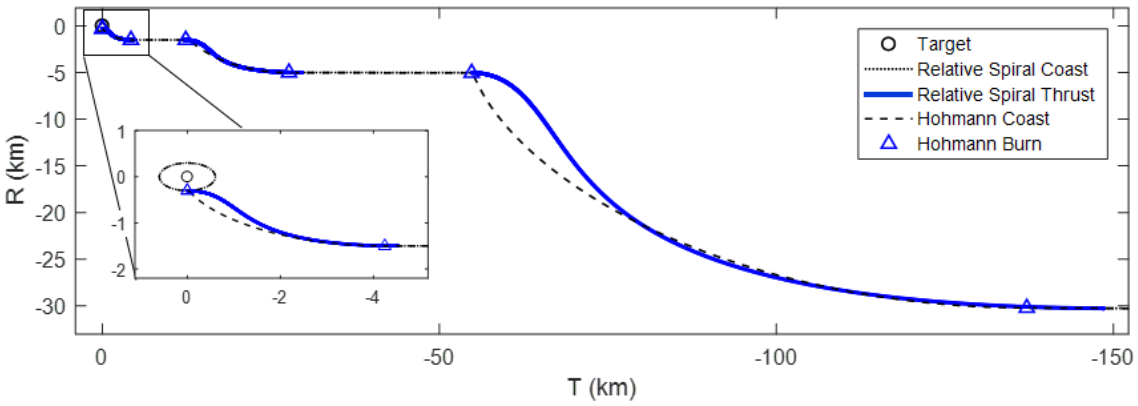

Figure 6. Comparison in target's RTN frame of low-thrust relative spiral trajectories and impulsive-thrust trajectories for GEO servicer orbit-raising sequence.

widely varying thrust profile represents an inefficient use of the power and propulsion systems. The large discrepancy in thrust magnitude between the first and subsequent maneuvers in Table 1 is caused by the large difference in transfer sizes and $n^2\delta r$ scaling of the thrust. This can be avoided by splitting the larger transfers into a series of smaller maneuvers. The new sequence will require more time and a larger initial separation, but will reduces the maximum thrust requirements with no change in fuel cost.

Formation Reconfiguration

After collecting sufficient situational awareness observations around the target, the servicer spacecraft performs a maneuver to reduce the size of its relative orbit. This is equivalent to reducing the servicer's orbit eccentricity and thus the relative eccentricity between servicer and target. Because closed, periodic relative motion is desired after the maneuver, the semimajor axis of the servicer's final orbit must match that of the target. Unlike the maneuvers considered in the previous section, the motion in this case is centered around the target and it may be treated as the chief for the analysis. There is no need to introduce artificial reference points and the simpler patching conditions in Eq. (18) apply.

The relative motion on a passive ellipse centered on the chief can be described analytically in terms of $\delta\theta$ and δr as

$$\delta v = \frac{1}{2} n \delta r \sqrt{1 + 15\cos^2\delta\theta} \tag{35}$$

$$\tan\delta\gamma = \frac{3\cos\delta\theta}{1 + 3\cos^2\delta\theta} \tag{36}$$

These equations define the boundary conditions for the patched spirals problem. In this example, the initial ellipse has a semiminor axis of 300 m and the final has a semiminor axis of 50 m. The dependence of δv on δr in Eq. (35) limits the applicability of the constant δv control strategy for this reconfiguration. If δv is to remain constant throughout the motion and if there can be no discontinuities in δv across the patch points, then the δv at departure from the first ellipse must equal that at arrival on the second. Two passive ellipses can only contain points with matching δv if the size ratio of larger to smaller is less than or equal to 2. For the ellipses selected in the sample problem, a spiral with constant δv cannot satisfy the patching conditions in Eq. (18) and the constant $\delta v/\delta r$ strategy must be adopted. According to Eq. (35), points on concentric passive ellipses that share a common $\delta v/\delta r$ must also share $\cos^2\delta\theta$. For any departure point on the initial ellipse, there are four compatible locations on the destination ellipse: two at $\delta\theta_0 + m\pi$ with relative flight path angle $\delta\gamma_0$ and two at $m\pi - \delta\theta_0$ with relative flight path angle $-\delta\gamma_0$.

First consider patching a single relative spiral between two ellipses. The only relative spiral trajectory which can satisfy the above constraints on the patch points is the logarithmic spiral with $\xi = 0$ and constant $\delta\gamma$. The ellipse and relative velocity constraints give $\delta\theta_f = \delta\theta_0 + m\pi$ and $\delta r_f/\delta r_0 = \delta r_{Ef}/\delta r_{E0}$, so Eqs. (27) and (36) become

$$\tan\delta\gamma_0 = \frac{1}{m\pi}\ln\frac{\delta r_{Ef}}{\delta r_{E0}} = \frac{3\cos\delta\theta_0\sin\delta\theta_0}{1 + 3\cos^2\delta\theta_0} \tag{37}$$

For a given ratio $\delta r_{Ef}/\delta r_{E0}$ and choice of m half-revolutions around the target, Eq. (37) has two solutions in the domain $(0, \pi)$ which are duplicated in $(\pi, 2\pi)$. These are illustrated in Figure 7(a) for the specified ellipse ratio and $m = 1$. The trajectory beginning at $\delta\theta_0$ nearer to $\pi/2$ is longer and has lower δv than the one beginning nearer to π, and they may be designated as the slow and fast solutions, respectively. Table 2 summarizes the performance of these trajectories along with the optimal impulsive solution for this reconfiguration.[28] As was the case for orbit raising, the fast spiral reconfiguration trajectory has a higher ΔV cost than its impulsive counterpart but may be accomplished with less propellant mass. An advantage of the continuous-thrust reconfiguration that was not evident in the orbit raising scenario is the substantial reduction in flight time. Using impulsive maneuvers, the flight time is governed by Keplerian dynamics. For the optimal three-impulse reconfiguration in GEO considered here, a full 24-hour orbital period is required. In contrast, the fast spiral trajectory completes the reconfiguration in just over 9 hours.

To achieve further improvements in flight time and ΔV, one may increase the number of spirals used in the reconfiguration maneuver. Doing so adds degrees of freedom to the problem, allowing for multiple

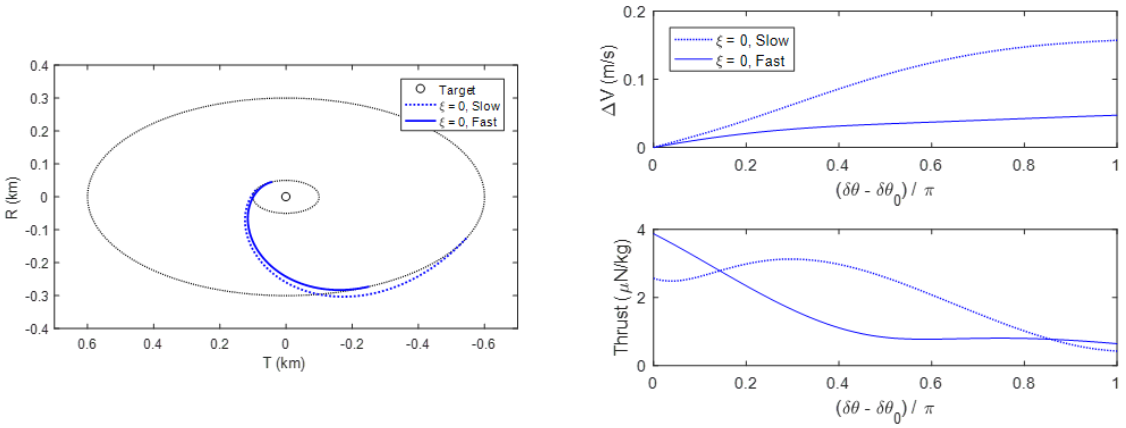

(a) Maneuver trajectory in RTN frame of target.

(b) Evolution of ΔV cost and thrust magnitude

Figure 7. Half-revolution, single-spiral reconfiguration from a passive ellipse with $\delta\mathbf{r_{E0}} = 300$ m to one with $\delta\mathbf{r_{Ef}} = 50$ m for a pair of spacecraft in GEO.

Table 2. Performance comparison for GEO servicer reconfiguration maneuvers.

	Impulsive Thrust (Isp 300 s)	Low-Thrust Relative Spirals (Isp 2000 s)		
		Single Spiral, $m = 1$		Double Spiral, $m = 1$
		Fast	Slow	
ΔV (cm/s)	0.91	4.73	15.73	4.04
Propellant (mg/kg s/c)	3.1	2.4	8.0	2.1
Max Thrust (μN/kg s/c)	-	3.9	3.1	6.3
Reconfiguration Time (h)	24.0	9.1	20.8	7.1

solutions and optimization. For the case of two spirals, for example, the restrictions imposed on $\delta\gamma$ and $\delta\theta$ by Eqs. (35) and (36) and the constant $\delta v/\delta r$ control strategy, the patching conditions in Eq. (18), and the geometric relationship in Eq. (27) result in a single constraint equation relating ξ_1 and ξ_2. For half-revolution, two-spiral reconfiguration of the ellipses prescribed by the GEO servicer example there is a shallow optimum in ΔV at $\delta\theta_0 = 0.8\pi$, $\xi_1 = -0.5$, $\xi_2 = -0.08$. Performance results for this trajectory are included with the single-spiral and impulsive reconfiguration results in Table 2. This two-spiral solution achieves a 15% improvement in ΔV over the fast, half-revolution single-spiral solution while reducing the reconfiguration time by 2 hours.

SENSITIVITY ANALYSIS

All simulation results presented thus far have assumed pure Keplerian motion, perfect thrust control, and perfect knowledge of the relative state. To validate the relative spiral trajectory analysis approach, it must be shown to produce acceptable results in high-fidelity simulation including all relevant perturbations and with realistic uncertainties in the state and control variables. Because these uncertainties will depend upon the spacecraft design, controller implementation, and mission profile, this study will examine the sensitivity of a representative trajectory solution to each source of error. This will provide a reference for the regime of validity of the trajectory solutions.

Relevant sources of error may be divided between three categories. First are errors related to the underlying assumptions of the analysis, namely that the chief is in a circular orbit and that the relative motion is restricted to the chief's orbital plane. The second are errors caused by uncertainties in the estimated state, which feed into the commanded thrust. Finally, actuation errors will be introduced by the spacecraft's thrusters and attitude control system. After a description of the test case and simulation setup, each of these sources is

Table 3. Simulation parameters

Parameter	Value
Integrator	Runge-Kutta (Dormand-Prince)
Time Step (s)	Fixed: 5 s
Gravity Model	GGM01S (8x8)
Solar Radiation Pressure	Cross-section normal to sun, no eclipses
ΔB_{SRP}	0.001
Third Body Effects	Moon and Sun Point Mass, Analytical Ephemerides

examined individually.

The contributions of each source of error are studied through high-fidelity numerical integration of the equations of motion in the MATLAB/Simulink environment.[29] The test case is based upon the fast, half-revolution reconfiguration maneuver described above for the GEO servicer mission scenario. The numerical integration propagates the Earth-centered inertial (ECI) coordinates of the chief and deputy subject to high-order Earth gravity, solar radiation pressure, relativistic effects, and third-body effects from the sun and moon. Table 3 details the relevant parameters for each as well as other important simulation parameters. Because the nominal orbit being studied is in GEO, there is no perturbation by atmospheric drag.

To provide a consistent set of geometric starting parameters for the simulation, initial conditions are specified in terms of orbit element sets. Because the scenario involves a near-circular equatorial orbit, the chief's quasi-nonsingular absolute orbit elements and the formation's nonsingular relative orbit elements (ROE) are used to initialize the absolute and relative motion, respectively. These are converted to the position and velocity vectors in ECI, which are concatenated to form the state vectors $\mathbf{x_{ECI}}$ of the chief and deputy for propagation as in Figure 8. The quasi-nonsingular absolute orbit elements are defined as

$$\mathbf{oe} = \begin{pmatrix} a \\ \lambda \\ e_x \\ e_y \\ i_x \\ i_y \end{pmatrix} = \begin{pmatrix} a \\ \omega + \Omega + M \\ e\cos(\omega + \Omega) \\ e\sin(\omega + \Omega) \\ \sin i \cos\Omega \\ \sin i \sin\Omega \end{pmatrix} \tag{38}$$

where a, e, i, ω, Ω, and M are the Keplerian orbital elements. Table 4 lists the initial conditions for the chief's orbit. For each parameter being studied, simulations are run for a range of mean anomalies to sample the effects of third body perturbations, higher-order gravity, and the chief's orbit eccentricity. The nonsingular ROE are defined by combinations of the classical orbital elements of the chief and deputy as[30]

$$\boldsymbol{\delta oe} = \begin{pmatrix} \delta a \\ \delta\lambda \\ \delta e_x \\ \delta e_y \\ \delta i_x \\ \delta i_y \end{pmatrix} = \begin{pmatrix} (a_d - a_c)/a_c \\ \lambda_d - \lambda_c \\ e_{dx} - e_{cx} \\ e_{dx} - e_{cx} \\ \frac{i_{dx}}{1+\cos i_d} - \frac{i_{cx}}{1+\cos i_c} \\ \frac{i_{dy}}{1+\cos i_d} - \frac{i_{cy}}{1+\cos i_c} \end{pmatrix} \tag{39}$$

Table 5 lists the nominal initial and target ROE states, which describe relative orbits centered on the chief. For a phase of the relative orbit given by $\delta\theta$ the values of δe_x and δe_y depend upon the mean anomaly, so Table 5 reports the magnitude of the relative eccentricity vector $\boldsymbol{\delta}\mathbf{e}$. When scaled by a_c, this value defines the semiminor axis of the passive elliptical relative motion. The sizes of the relative orbits have been increased

Table 4. Nominal initial conditions for the chief absolute orbit

a_c (km)	e_{cx}	e_{cy}	i_{cx}	i_{cy}	λ_c (deg)
42164	-0.0001	0	0	0.002	[0:15:345]

Table 5. Nominal initial and target final conditions for the relative orbit of deputy around chief

	$a_c\delta a$ (m)	$a_c\delta\lambda$ (m)	$a_c \|\boldsymbol{\delta}\mathbf{e}\|$ (m)	$a_c\delta i_x$ (m)	$a_c\delta i_y$ (m)
Initial	0	0	1000	0	0
Final	0	0	250	0	0

from those in the mission scenario described above to provide a better baseline for the sensitivity analysis. The nominal minimum separation on the initial and final passive ellipses are therefore 1000 m and 250 m, respectively.

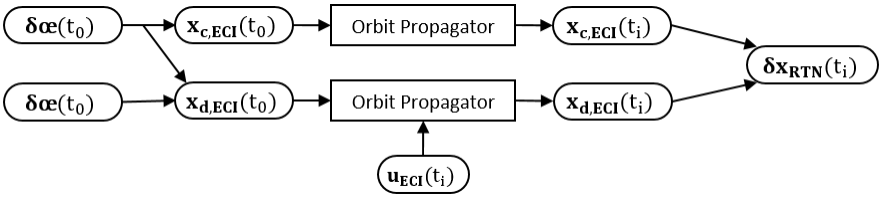

Figure 8. Schematic illustration of simulation strategy.

For the purpose of sensitivity analysis, the controller governing $\mathbf{u_{ECI}}$ in Figure 8 is implemented as an open-loop control law in the simulation. Figure 9 illustrates the flow of information through the controller. The relative state is read by the controller at the beginning of the simulation, which coincides with the start of the maneuver. The relative state vector $\boldsymbol{\delta}\mathbf{x}_{\boldsymbol{\theta\gamma}} = (\delta r,\, \delta\theta,\, \delta v,\, \delta\gamma)$ is then computed from $\boldsymbol{\delta}\mathbf{x}_{\mathbf{RTN}}$. In the nominal simulation scenario, perfect knowledge of the relative state is assumed in this calculation to avoid compounding errors and obscuring sensitivity results. The predicted relative state vector is updated according to the trajectory solution geometry in Eq. (9), then used to compute the components of thrust from Eqs. (8) and (13). Finally the control thrust $\mathbf{u_{ECI}}(t_i)$ is obtained by rotating the RTN components of thrust in accordance with the initial RTN to ECI transformation and the assumptions of a circular chief orbit and coplanar motion.

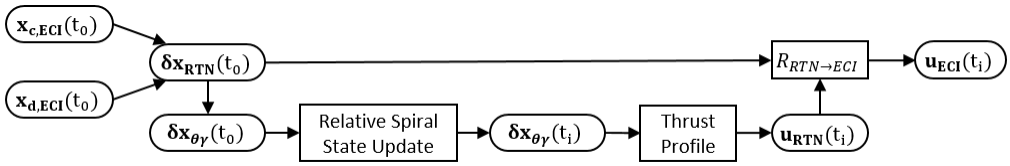

Figure 9. Implementation of relative spiral control law in open-loop for sensitivity analysis.

For direct comparison of the sensitivity to changes in individual inputs, a metric characterizing the raw error in the final state is convenient. This study adopts the error index proposed by Sullivan et al. for the assessment of relative dynamics models.[31] It is defined by the maximum L_2-norm of the difference between the true and expected values of the relative state vector $\boldsymbol{\delta}\mathbf{x}_{\mathbf{RTN}}$ formed by concatenating the relative position and relative velocity vectors in the RTN frame. The true state is computed from the propagated ECI states of the chief and deputy in Figure 8, while the expected state is obtained from the relative spiral trajectory solution through the state vector $\boldsymbol{\delta}\mathbf{x}_{\boldsymbol{\theta\gamma}}$. The raw error index is then calculated as

$$\varepsilon = \max_i \left\| W\left(\boldsymbol{\delta}\mathbf{x}_{\mathbf{RTN,true}}(t_i) - \boldsymbol{\delta}\mathbf{x}_{\mathbf{RTN,ref}}(t_i)\right)\right\|_2 \tag{40}$$

where W is the weight matrix $\mathrm{diag}(1, 1, 1, n^{-1}, n^{-1}, n^{-1})$ which scales the relative velocity and gives it dimensions of length.

Two additional metrics are relevant to the reconfiguration scenario being considered. One is the final mean relative semimajor axis, δa, defined in Eq. (39). The desired final state is a passive ellipse centered on the

chief, implying that the orbit energies of the chief and deputy are matched and therefore the final value of δa is zero. In the absence of thrust, a nonzero value of δa will lead to along-track drift of the relative motion, as seen in the formation establishment phase of the GEO servicer mission scenario. The second metric is the final magnitude of the relative eccentricity vector $\|\boldsymbol{\delta}\mathbf{e}\|$. As specified in Table 5, the scaled magnitude of the relative eccentricity vector at the end of the maneuver should be 250 m. Departures from this value result in a discrepancy between the desired and realized minimum in-plane separation between the two spacecraft.

Deviation from Assumptions

Real mission scenarios will not perfectly match the conditions used to derive the thrust profile in Eqs. (8), (13), and (15). The reference orbit cannot be perfectly circular, the chief and deputy will have nonzero separation, and there will always be some out-of-plane motion. The sensitivity of the reconfiguration scenario to these three nonidealities are illustrated in Figures 10, 11, and 12, respectively. The solid line gives the metric's average value over the full range of mean anomalies with the dashed lines marking the mean plus and minus one standard deviation.

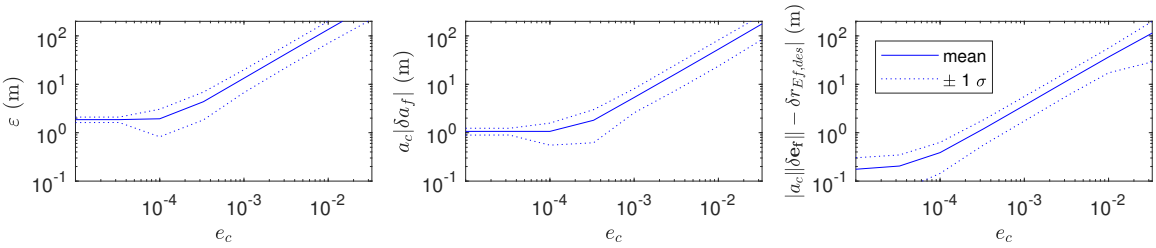

Figure 10. Effect of nonzero chief eccentricity on the raw error index (left) and errors in the final mean relative semimajor axis (middle) and relative eccentricity (right).

Figure 10 shows that large errors result for chief orbits with eccentricities above 0.001 in this reconfiguration scenario. Furthermore, an error on the order of 1 m in relative semimajor axis remains in the limit of a circular chief orbit. This error is caused by gravitational perturbations on the relative motion, as evidenced by the middle plot of Figure 11. As the size of the initial relative orbit decreases toward zero, the error is reduced by more than an order of magnitude. This residual error is due to perturbations which are independent of separation, such as differential solar radiation pressure.

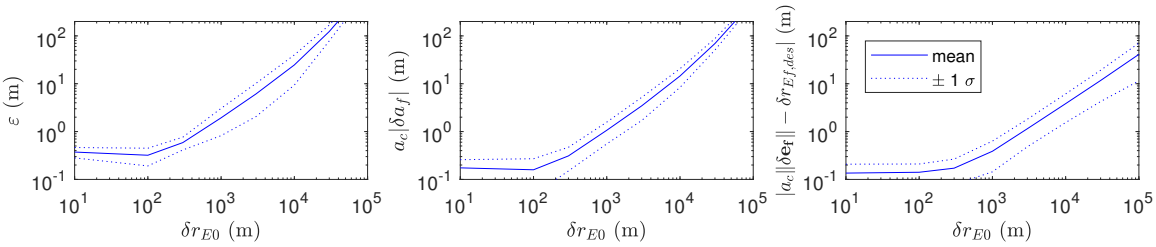

Figure 11. Effect of relative orbit size on the raw error index (left) and errors in the final mean relative semimajor axis (middle) and relative eccentricity (right).

The sensitivity to out-of-plane motion is illustrated by Figure 12 which shows the effect of a difference in inclination δi_y. Although the raw error index suggests a significant sensitivity for $a_c \delta i_{y,0}$ greater than 10 m, comparison with the other two metrics shows that the observed error is only the persistence of the initial out-of-plane motion. This result emphasizes the decoupling which motivated the focus on in-plane motion at the start of the analysis.

The selection of a test case in GEO was based upon both the commercial value of formation flying in this orbit regime and the n^2 scaling of the thrust profile. As an unintentional consequence, the perturbation environment is comparatively quiescent. Without large contributions from higher-order gravity or atmospheric

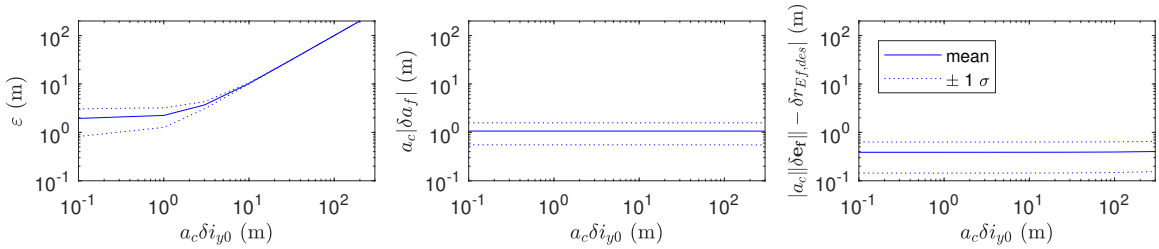

Figure 12. Effect of error in relative inclination on the raw error index (left) and errors in the final mean relative semimajor axis (middle) and relative eccentricity (right).

drag, solar radiation pressure is the most significant perturbation in this orbit. A difference of approximately 10% between the solar ballistic coefficients of chief and deputy was assumed for the nominal test case. This is based on the assumption that the deputy may be able to actively change its reflective area to match that of the chief and reduce the effect of this perturbation. Nevertheless, this perturbation is a large contributor to the offset in the error metrics as the other error sources vanish.

Uncertainty in State Estimate

The deputy's thrust profile is specified as a function of the relative state variables and any implementation of it will depend on estimates or measurements of those variables and their uncertainties. In the open-loop implementation of the control law in Figure 9, an estimate of the relative state at the beginning of the maneuver is used to propagate the state forward based on the analytical solution for the trajectory shape. The sensitivity of the final motion to uncertainty in this initial estimate is shown in Figure 13. As in the other sensitivity tests, the nominal relative state in Table 5 was used as the initial estimate in the controller. To model uncertainty in this estimate, the true initial state was obtained from this nominal state by adding normally-distributed random errors to the equivalent RTN relative state vector $\boldsymbol{\delta}\mathbf{x}_{\mathbf{RTN}}$. The metrics in Figure 13 are plotted against the standard deviation of the estimate error. For each value of the error spread, a total of 48 simulations were run and their mean and standard deviations are shown in the figure. As was done in the definition of the raw error index ε, errors in velocity have been scaled by the mean motion n to have dimensions of length.

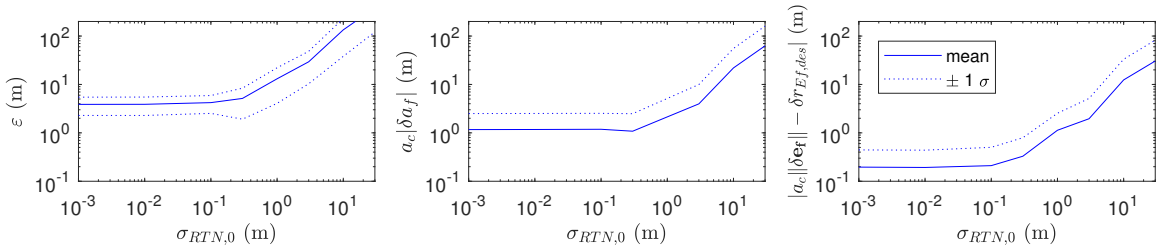

Figure 13. Effect of uncertainty in initial relative state on the raw error index (left) and errors in the final mean relative semimajor axis (middle) and relative eccentricity (right).

From Figure 13 it is clear that uncertainties larger than a few meters in the initial relative state can lead to significant errors in the final state. A closed-loop implementation of the thrust profile would improve the situation by preventing error propagation. Small deviations from the predicted relative trajectory would lead to a new desired relative spiral trajectory with a slightly modified thrust parameter ξ.

Error in Control Actuation

The last source of error for study is that due to the actuators. This category can be subdivided between effects of the attitude control on the thrust direction and effects of the thruster hardware on thrust magnitude. First consider the effect of thrust direction. The sensitivity test case assumes that the spacecraft's attitude is well-known and well-controlled, so that there is no bias away from the desired thrust direction. Instead, the thrust vector fluctuates around the desired direction with normally-distributed noise due to actuation errors and perturbing torques. Figure 14 shows the sensitivity to noise sampled at 5-minute intervals. The error metrics are plotted against the standard deviation of the noise angles, σ_α, in a 3-axis, small-angle rotation of the thrust vector. High-frequency noise would provide a good approximation of the desired thrust direction. The sample rate for the noise was therefore set much lower than the simulation step size to represents a more sluggish response by the attitude control system. The plotted results represent the mean and standard deviations of 48 simulations at each noise level.

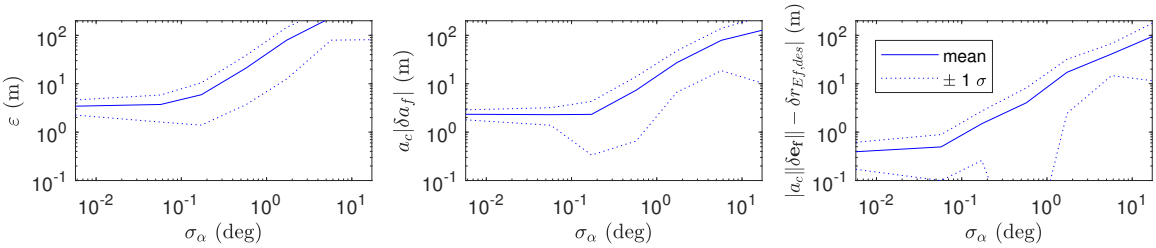

Figure 14. Effect of variation in thrust direction on the raw error index (left) and errors in the final mean relative semimajor axis (middle) and relative eccentricity (right).

A similar approach was applied to the analysis of errors in thrust magnitude. Figure 15 shows the sensitivity to normally-distributed fluctuations in thrust magnitude, sampled at 5-minute intervals. In this case, the noise represents a fractional offset from the desired thrust. As with the direction, the solution is more sensitive to low-frequency fluctuations which resemble a bias. Figure 16 examines the situation where there is a real bias in the magnitude of thrust, equal to the standard deviation of the noise. The effect of a bias in thrust is similar to that of an error in the initial state estimate as described in the previous section. Consequently, this error could also be improved by a closed-loop implementation which continuously or periodically updates the thrust parameter to compensate for deviations from the expected trajectory.

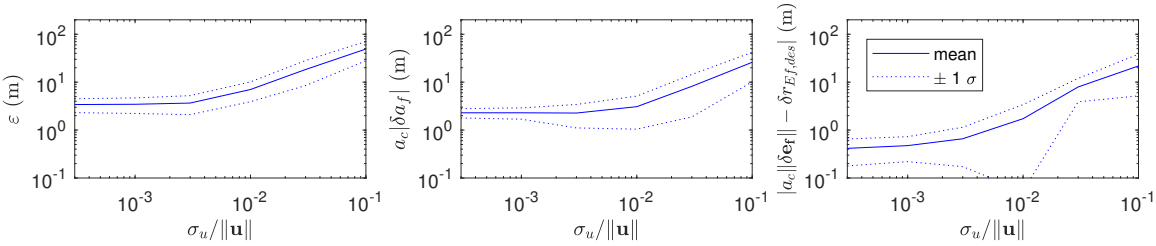

Figure 15. Effect of variation in thrust magnitude on the raw error index (left) and errors in the final mean relative semimajor axis (middle) and relative eccentricity (right).

This analysis has provided several key results. First, the relative spiral trajectory solutions are valid within the orbital regime for which the thrust profile is feasible. This has been demonstrated through open-loop implementation of a thrust controller based on the relative spiral solutions and simulated with all relevant perturbations. Second, the solution is very sensitive to the chief's orbital eccentricity and the size of the formation (cf. Figures 10 and 11). With some knowledge of the chief's orbital eccentricity vector, this source of error could be substantially reduced by modification of the feed-forward terms in Eqs. (8), (13), and (15).

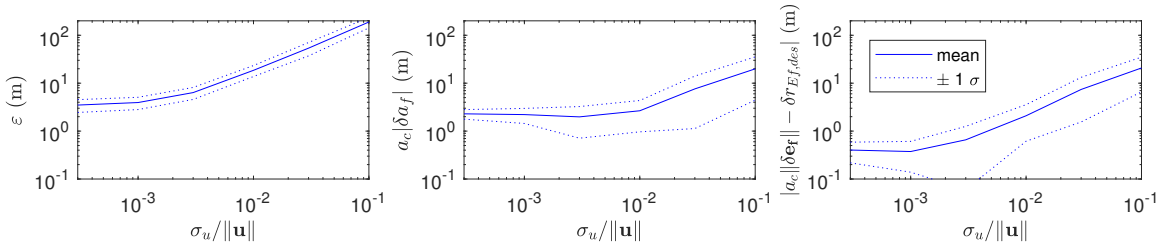

Figure 16. Effect of thrust offset with low-frequency variation on the raw error index (left) and errors in the final mean relative semimajor axis (middle) and relative eccentricity (right).

Next, the in-plane trajectory is insensitive to motions out of the chief's orbit plane. This observation is consistent with the results of linearized relative motion theory and justifies the focus on in-plane motion for this investigation. Finally, the sensitivity to errors in the state estimate and actuation suggest the need for a closed-loop implementation. As the deputy deviates from the path prescribed by the relative spiral trajectory solution, the controller solves the patched spirals constraints based on the new boundary conditions. It then updates the thrust parameter to drive the formation toward the desired final state.

CONCLUSION

This work has introduced the shape-based method of low-thrust trajectory design to the problem of relative motion for two spacecraft. The prescribed thrust profile yields a family of sinusoidal spiral trajectories characterized by the thrust parameter. This family exhibits sufficient variability to generate practical low-thrust trajectories for mission scenarios of interest while providing an analytical handle and geometric insights for design and optimization.

Two approaches were presented for controlling the relative velocity. In one the velocity is kept constant throughout the motion, while in the second the velocity varies in proportion to the separation. Because the thrust magnitude scales as $n^2\delta r$ in each case, the techniques outlined are most practical for medium earth orbit and GEO orbits. The example of a servicer spacecraft visiting a target in GEO was used to demonstrate two approaches to patching spiral trajectories and illustrated the utility of the control schemes considered. The constant δv strategy has merit for orbit raising in the virtual chief framework, while the constant $\delta v/\delta r$ approach enables reconfiguration of the formation state. When compared to impulsive transfers, both strategies may be used in their respective domains to reduce flight time. This is a large advantage for high altitude orbits in which the natural period may be considerably longer than the timescale of interest.

The sensitivity of the relative spiral trajectories to deviations from the underlying assumptions and to errors in the state estimate or thrust vector were studied. With moderately accurate thrust control and state estimates, the trajectory solutions provide a good approximation of the true trajectory in a realistic perturbation environment. Sensitivity to thrust and state estimates may be mitigated through a closed-loop implementation that adjusts the thrust parameter in real time. Although the thrust profiles were derived for coplanar relative motion around a circular reference orbit, they may be easily extended to handle out-of-plane motions and elliptical reference orbits. Further efforts should investigate the optimality conditions for maneuver design within the relative spiral framework and develop new relative velocity control schemes accordingly.

NOTATION

Vectors

$\mathbf{r}$	Position from central body	$\boldsymbol{\delta}\mathbf{r}$	Position of deputy from chief
$\mathbf{u}$	Thrust per unit mass	$\boldsymbol{\delta}\mathbf{v}$	Relative velocity in rotating RTN frame
$\mathbf{v}$	Velocity in inertial frame IJK	$\boldsymbol{\delta}\mathbf{x}$	Relative state vector
$\mathbf{x}$	Absolute state vector	$\delta\hat{\boldsymbol{\gamma}}$	$\hat{\boldsymbol{\omega}} \times \boldsymbol{\delta}\hat{\mathbf{v}}$
$\boldsymbol{\delta\text{œ}}$	Relative orbit elements	$\boldsymbol{\delta}\hat{\boldsymbol{\theta}}$	$\boldsymbol{\delta}\hat{\mathbf{r}} \times \hat{\boldsymbol{\omega}}$
$\boldsymbol{\delta}\mathbf{e}$	Relative eccentricity vector	$\hat{\boldsymbol{\theta}}$	$\hat{\boldsymbol{\omega}} \times \hat{\mathbf{r}}$
$\boldsymbol{\delta}\mathbf{i}$	Relative inclination vector	$\boldsymbol{\omega}$	Angular velocity of RTN frame in IJK

Parameters

a	Semimajor axis	δi	Relative inclination
B_{SRP}	Ballistic coefficient for SRP	δr	Deputy separation from chief
e	Eccentricity	δv	Deputy speed relative to chief in RTN
i	Inclination	$\delta\gamma$	Deputy flight path angle in RTN
M	Mean motion	$\delta\lambda$	Relative longitude
n	Chief mean motion	$\delta\theta$	Deputy azimuth from chief radial direction
r	Radial distance to central body	ΔV	Change in inertial velocity due to thrust
R	Projection of $\boldsymbol{\delta}\mathbf{r}$ onto $\hat{\mathbf{r}}$ of chief	ε	Error index
t	Time	λ	Mean latitude
T	Projection of $\boldsymbol{\delta}\mathbf{r}$ onto $\hat{\boldsymbol{\theta}}$ of chief	μ	Gravity parameter of central body
v	Speed in inertial frame	σ	Standard deviation
TOF	Time of flight	ξ	Thrust parameter
δa	Relative semimajor axis	ω	argument of perigee
δe	Relative eccentricity	Ω	Right ascension of the ascending node

Scripts

0	Initial	r	Radial measure of vector
c	Chief	RTN	Radial-transverse-normal coordinates
d	Deputy	t	Transverse measure of vector
E	Passive ellipse in RTN frame	x	$\hat{\mathbf{x}}$-measure of vector
ECI	Earth-centered inertial coordinates	y	$\hat{\mathbf{y}}$-measure of vector
f	Final	α	Perturbation angle
i	Arbitrary step in simulation	$\theta\gamma$	Absolute or relative polar coordinates
IJK	Arbitrary inertial reference frame	$+$	After patch
m	Minimum or maximum	$-$	Before patch

REFERENCES

[1] C. Chouinard, R. Knight, G. Jones, D. Tran, and D. Koblick, "Automated and Adaptive Mission Planning for Orbital Express," SpaceOps 2008, Heidelberg, Germany, May 12-16, 2008.

[2] J.-S. Ardaens and S. D'Amico, "Spaceborne Autonomous Relative Control System for Dual Satellite Formations," *Journal of Guidance, Control, and Dynamics*, Vol. 32, No. 6, 2009, pp. 1859–1870.

[3] S. D'Amico, J.-S. Ardaens, and R. Larsson, "Spaceborn Autonomous Formation-Flying Experiment on the PRISMA Mission," *Journal of Guidance, Control, and Dynamics*, Vol. 35, No. 3, 2012, pp. 834–850.

[4] S. D'Amico, M. Pavone, S. Saraf, A. Alhussien, T. Al-Saud, S. Buchman, R. Bryer, and C. Farhat, "Distributed Space Systems for Future Science and Exploration," 8th International Workshop on Spacecraft Formation Flying, Delft University, June 8-10, 2015.

[5] J. E. Polk, R. Y. Kakuda, J. R. Anderson, J. R. Brophy, V. K. Rawlin, M. J. Patterson, J. Sovey, and J. Hamley, "Validation of the NSTAR Ion Propulsion System on the Deep Space One Mission: Overview and Initial Results," 35th AIAA/ASME/SAE/ASEE Joint Propulsion Conference, Los Angeles, CA, June 20-24, 1999.

[6] C. E. Garner, M. M. Rayman, G. J. Whiffen, J. R. Brophy, and S. C. Mikes, "Ion Propulsion: An Enabling Technology for the Dawn Mission," 23rd AAS/AIAA Spaceflight Mechanics Meeting, Kauai, Hawaii, February 10-14, 2013.
[7] C. Casaregola, "Electric Propulsion for Station Keeping and Electric Orbit Raising on Eutelsat Platforms," 30th International Symposium on Space Technology and Science, Hyogo-Kobe, Japan, July 4-10, 2015.
[8] G. P. Sutton and O. Biblarz, *Rocket Propulsion Elements*. John Wiley & Sons, 1st ed., 2010.
[9] D. M. Goebel and I. Katz, *Fundamentals of Electric Propulsion: Ion and Hall Thrusters*. John Wiley & Sons, 1st ed., 2008.
[10] C. Lembeck and J. Prussing, "Optimal Impulsive Intercept with Low-Thrust Rendezvous Return," *Journal of Guidance, Control, and Dynamics*, Vol. 16, No. 3, 1993, pp. 426–433.
[11] T. E. Carter, "Optimal power-limited rendezvous of a spacecraft with bounded thrust and general linear equations of motion," *Journal of Optimization Theory and Applications*, Vol. 87, No. 3, 1995, pp. 487–515.
[12] M. Guelman and M. Aleshin, "Optimal Bounded Low-Thrust Rendezvous with Fixed Terminal Approach Direction," *Journal of Guidance, Control, and Dynamics*, Vol. 24, No. 2, 2001, pp. 378–385.
[13] D. F. Lawden, *Optimal Trajectories for Space Navigation*. Butterworths, 1963.
[14] M. S. d. Queiroz, V. Kapila, and Q. Yan, "Adaptive Nonlinear Control of Multiple Spacecraft Formation Flying," *Journal of Guidance, Control, and Dynamics*, Vol. 23, No. 3, 2000, pp. 385–390.
[15] H. Schaub, S. R. Vadali, J. L. Junkins, and K. T. Alfriend, "Spacecraft Formation Flying Control using Mean Orbit Elements," *AAS Journal of the Astronautical Sciences*, Vol. 48, No. 1, 2000, pp. 69–87.
[16] K. Schilling, P. Bangert, and S. B. e. al., "NetSat: a four pico/nano-satellite mission for demonstration of autonomous formation flying," 66th International Astronautical Congress, Jerusalem, Israel, October 12-16, 2015.
[17] L. M. Steindorf, S. D'Amico, J. Scharnagl, F. Kempf, and K. Schilling, "Constrained Low-Thrust Satellite Formation-Flying using Relative Orbit Elements," 27th AAS/AIAA Space Flight Mechanics Meeting, San Antonio, Texas, February 5-9, 2017.
[18] R. Bevilacqua and T. A. Lovell, "Analytical guidance for spacecraft relative motion under constant thrust using relative orbit elements," 23rd AAS/AIAA Space Flight Mechanics Meeting, Kauai, Hawaii, February 10-14, 2013.
[19] R. H. Bacon, "Logarithmic Spiral: An Ideal Trajectory for the Interplanetary Vehicle with Engines of Low Sustained Thrust," *American Journal of Physics*, Vol. 27, No. 3, 1959, pp. 164–165.
[20] A. E. Petropoulos and J. M. Longuski, "Shape-Based Algorithm for the Automated Design of Low-Thrust, Gravity Assist Trajectories," *Journal of Spacecraft and Rockets*, Vol. 41, No. 5, 2004, pp. 787–796.
[21] J. Roa, J. Pelaez, and J. Senent, "New Analytic Solution with Continuous Thrust: Generalized Logarithmic Spirals," *Journal of Guidance, Control, and Dynamics*, Vol. 39, No. 10, 2016, pp. 2336–2351.
[22] M. Willis and S. D'Amico, "Relative Spiral Trajectories for Low-Thrust Formation Flying," 26th International Symposium on Space Flight Dynamics, Matsuyama, Japan, June 3-9, 2017.
[23] W. H. Clohessy and R. S. Wiltshire, "Terminal Guidance System for Satellite Rendezvous," *Journal of Guidance, Control, and Dynamics*, Vol. 27, No. 9, 1960, pp. 653–658.
[24] J. D. Lawrence, *A Catalog of Special Plane Curves*. Dover Publications, 1972.
[25] M. Abramowitz and I. A. Stegun, *Handbook of Mathematical Functions: With Formulas, Graphs, and Mathematical Tables*. Dover Publications, 1970.
[26] R. E. Sherrill, A. J. Sinclair, T. A. Lovell, K. W. Johnson, and D. D. Decker, "The Virtual-Chief Method for Modeling Relative Motion of Noncircular Satellites," 21st AAS/AIAA Space Flight Mechanics Meeting, New Orleans, Louisiana, 2011.
[27] B. W. Barbee, J. R. Carpenter, and S. H. e. al, "A Guidance and Navigation Strategy for Rendezvous and Proximity Operations with a Noncooperative Spacecraft in Geosynchronous orbit," *Journal of the Astronautical Sciences*, Vol. 58, No. 3, 2011, pp. 389–408.
[28] M. Chernick and S. D'Amico, "New Closed-Form Solutions for Optimal Impulsive Control of Spacecraft Relative Motion," AIAA/AAS Astrodynamics Specialist Conference, Long Beach, CA, September 13-16, 2016.
[29] D. Eddy, V. Giralo, and S. D'Amico, "Development and Verification of the Stanford GNSS Navigation Testbed for Spacecraft Formation-Flying," Technical Note, 2017. URL: https://people.stanford.edu/damicos/sites/default/files/tn2017_eddygiralodamico.pdf.
[30] A. Koenig, T. Guffanti, and S. D'Amico, "New State Transition Matrices for Spacecraft Relative Motion in Perturbed Orbits," *Journal of Guidance, Control, and Dynamics*, 2017. Accepted.
[31] J. Sullivan, S. Grimberg, and S. D'Amico, "Comprehensive Survey and Assessment of Spacecraft Relative Motion Dynamics Models," *Journal of Guidance, Control, and Dynamics*, 2017. Accepted.